

# Comparison of 32 x 128 and 32 x 32 Geiger-mode APD FPAs for single photon 3D LADAR imaging

Mark A. Itzler\*, Mark Entwistle, Mark Owens, Ketan Patel, Xudong Jiang, Krystyna Slomkowski, and Sabbir Rangwala

Princeton Lightwave Inc., 2555 US Route 130 South, Cranbury, NJ 08512

Peter F. Zalud, Tom Senko, John Tower, and Joseph Ferraro  
Sarnoff Corp., 201 Washington Road, Princeton, NJ 08543

## ABSTRACT

We present results obtained from 3D imaging focal plane arrays (FPAs) employing planar-geometry InGaAsP/InP Geiger-mode avalanche photodiodes (GmAPDs) with high-efficiency single photon sensitivity at 1.06  $\mu\text{m}$ . We report results obtained for new 32 x 128 format FPAs with 50  $\mu\text{m}$  pitch and compare these results to those obtained for 32 x 32 format FPAs with 100  $\mu\text{m}$  pitch. We show excellent pixel-level yield—including 100% pixel operability—for both formats. The dark count rate (DCR) and photon detection efficiency (PDE) performance is found to be similar for both types of arrays, including the fundamental DCR vs. PDE tradeoff. The optical crosstalk due to photon emission induced by pixel-level avalanche detection events is found to be qualitatively similar for both formats, with some crosstalk metrics for the 32 x 128 format found to be moderately elevated relative to the 32 x 32 FPA results. Timing jitter measurements are also reported for the 32 x 128 FPAs.

**Keywords:** avalanche photodiode, single photon detector, photon counting, Geiger-mode, ladar, three-dimensional imaging, LADAR imaging, InP, InGaAsP

## 1. INTRODUCTION

One of the most promising current trends in advanced imaging is progress in the development of three-dimensional imaging techniques. Three-dimensional image data enables superior object recognition and identification by eliminating the ambiguities present in conventional two-dimensional (2D) intensity images. Three-dimensional (3D) imagery with high-resolution range (i.e., depth) information can be obtained using time-of-flight laser ranging and detection (LADAR) techniques. In addition to superiority over 2D imaging, this use of short laser pulses of ns-scale duration also provides much higher resolution imaging than longer wavelength sensing techniques (e.g., radar).

Most LADAR imaging systems in use today are based on the scanning of a single detector over the scene to be imaged. A separate laser pulse must be launched and pulse returns detected for each pixel of the image. Acquiring 3D images a single pixel at a time is time-consuming and can lack accuracy in the merging of the individual pixel data. As in the evolution of forward-looking infrared imaging—in which single-pixel scanning approaches gave way to linear-array pushbroom techniques, followed by the eventual deployment of large pixel-count area arrays—systems for 3D imaging will inevitably migrate to array-based sensors.

The use of arrays with pixels consisting of Geiger-mode avalanche diodes (GmAPDs) [1,2] provides several benefits for LADAR 3D imaging applications [3]. These detectors have single photon sensitivity and thus provide high efficiency detection for highly attenuated return signals. With single photon sensitivity at the imager pixels, the pulse energy requirements for launched LADAR pulses are greatly reduced relative to other detector technologies and lead to much more deployable and reliable system solutions. Moreover, the Geiger mode detection process is inherently digital: in these detectors, a single photon induces a macroscopic pulse of current that can be readily sensed with appropriate threshold detection circuitry. Given the digital nature of this detection mechanism, the detection process is noiseless; the only FPA-level noise is from the shot noise associated with false counts resulting from background or dark count mechanisms. This imager architecture is also realized with efficient “photons-to-bits” digital pixel circuitry that

\*mitzler@princetonlightwave.com; tel: 1.609.495.2551; www.princetonlightwave.com

This work was sponsored by the Defense Advanced Research Projects Agency under contract HR0011-08-C-0021. Approved for Public Release, Distribution Unlimited. The views, opinions, and/or findings contained in this article are those of the author and should not be interpreted as representing the official views or policies, either expressed or implied, of the Defense Advanced Research Projects Agency or the Department of Defense.

provides excellent prospects for scaling to smaller pitch and larger formats.

With the goal of demonstrating such scaling, in this paper we present results for the first 32 x 128 focal plane arrays (FPAs) based on planar-geometry GmAPDs [4]. These new FPAs employ design and fabrication platforms previously established by the authors for 32 x 32 FPAs [5–7]. Beyond the increase in pixel count, the new 32 x 128 FPAs employ pixels on a 50  $\mu\text{m}$  pitch, which represents a factor of two reduction relative to the 100  $\mu\text{m}$  pitch pixels realized on our earlier 32 x 32 format FPAs. Such a substantial pitch reduction has been demonstrated previously using similar architectures for the read-out electronics with mesa-geometry GmAPDs [8], and our current work confirms the viability of the planar-geometry devices on this length scale. For the most salient performance characteristics of these GmAPD FPAs, we compare results obtained for 32 x 32 x 100  $\mu\text{m}$  pitch sensors with our new 32 x 128 x 50  $\mu\text{m}$  pitch FPAs. Section 2 contains an overview of the device technologies incorporated in the FPA along with a description of the FPA module design. In Section 3, we illustrate full-array performance maps and statistical analysis of the dark count rate (DCR) and photon detection efficiency (PDE) for FPAs of both formats, as well as the fundamental trade-off between DCR vs. PDE in both sensor types. Characterization results for optical crosstalk in the two FPA formats are compared in Section 4, and a summary of the timing jitter performance of the 32 x 128 FPA is contained in Section 5. In Section 6, we sum up the results of this work.

## 2. FOCAL PLANE ARRAY DESIGN CONCEPT

### 2.1 Geiger-mode avalanche photodiode (GmAPD) arrays

When an avalanche photodetector is biased above its breakdown voltage  $V_b$ , the creation of a single electrical carrier can induce a run-away avalanche that gives rise to a detectable macroscopic current. In this mode of operation, often referred to as Geiger mode, the detector is sensitive to the absorption of a single photon. (For this reason, these detectors are also often referred to as single photon avalanche diodes, or SPADs.) We have developed InGaAs/InP avalanche diode structures specifically for single photon detection in the wavelength range of 0.92 to 1.67  $\mu\text{m}$  [9], and we have optimized this structure for shorter wavelength operation 1.06  $\mu\text{m}$  by employing a quaternary InGaAsP absorber in place of the longer wavelength ternary InGaAs absorber. [10] We have described in detail the design, simulation, and characterization of discrete GmAPD devices employing both InGaAs and InGaAsP absorption regions in previous publications [4,9–12].

A schematic depiction of the GmAPD device structure is illustrated in Figure 1(a). For the FPAs described in this paper, photon absorption occurs in a quaternary InGaAsP layer ( $E_g \sim 1.03$  eV) optimized for detection of single photons at 1.06  $\mu\text{m}$ . The absorption layer is spatially separated from a wider bandgap InP region ( $E_g \sim 1.35$  eV) in which avalanche multiplication occurs. A primary goal of the design—the separate absorption and multiplication (SAM) region structure [13]—is to maintain low electric field in the narrower bandgap absorber (to avoid dark carriers due to tunneling) while maintaining sufficiently high electric field in the multiplication region (so that impact ionization leads to significant avalanche multiplication). The creation of a single electron-hole pair by photoexcitation in the absorber layer results in the injection of the hole into the high-field InP multiplication region in which impact ionization results in avalanche gain. With the GmAPD biased above  $V_b$  in its armed state, the resulting avalanche gives rise to a macroscopic current pulse that is sufficiently large to be sensed by a threshold detection circuit contained in the readout integrated circuit. Unlike linear mode APDs operated below  $V_b$ , the GmAPD detection process is inherently digital, and with appropriately designed detectors and threshold circuits, the detection process is noiseless.

The lateral structure of our design employs a buried p-n junction to guarantee edge breakdown suppression, low perimeter leakage, and high reliability. The active area of this planar geometry device [14] is determined by the patterning of a SiN dielectric passivation layer to create a diffusion mask for a subsequent diffusion of Zn dopant atoms to create a  $p^+$ -InP region within the i-InP cap layer. To suppress electric field enhancement at the edge of this planar structure, we use two diffusions to tailor the p-n junction profile [15] so that the junction is deeper in the central part of the active area than it is in the junction periphery. This design ensures that the gain profile across the center part of the active region is uniform and that the gain is reduced in the peripheral region of the device. For 32 x 32 and 32 x 128 formats described in this paper, the optical active region diameters in each pixel are 34  $\mu\text{m}$  and 18  $\mu\text{m}$ , respectively.

### 2.2 CMOS Readout integrated circuit (ROIC) functionality

The basic functions of our 3D imaging FPA are performed by a custom CMOS ROIC mated to the GmAPD photodiode array (PDA) by indium bump hybridization. In the disarmed state, every pixel of the detector array is biased slightly

below the breakdown voltage of the GmAPD using a single external low-noise voltage supply with voltages on the order of 70 to 80 V. Each imaging frame begins with the arming of all of the detector pixels by the ROIC, which applies an excess bias of up to 5 V. The period during which the pixels remained armed is the range gate, which is typically on the order of a few microseconds. In a LADAR imaging system, the beginning of the range gate is synchronized (up to a fixed delay) with the launch of an optical pulse from which reflected photons will be detected. Every pixel contains a pseudorandom counter that provides detection timing information on a per-pixel basis. Upon asserting the master clock enable (MCE) signal, all pixel counters begin counting. Within each ROIC pixel, there is a threshold detection circuit that is triggered when an avalanche event occurs in the corresponding armed pixel of the photodiode array. When a detection occurs, an active quenching circuit removes the excess bias from the fired GmAPD pixel to disarm it, and the in-pixel counter is stopped so that the time of detection within the range gate is recorded. At the end of each range gate, pixels that do not sense an avalanche event record the terminal counter value, indicating that no event has occurred at that pixel. The frame readout then consists of scanning out all of the pixel counter values.

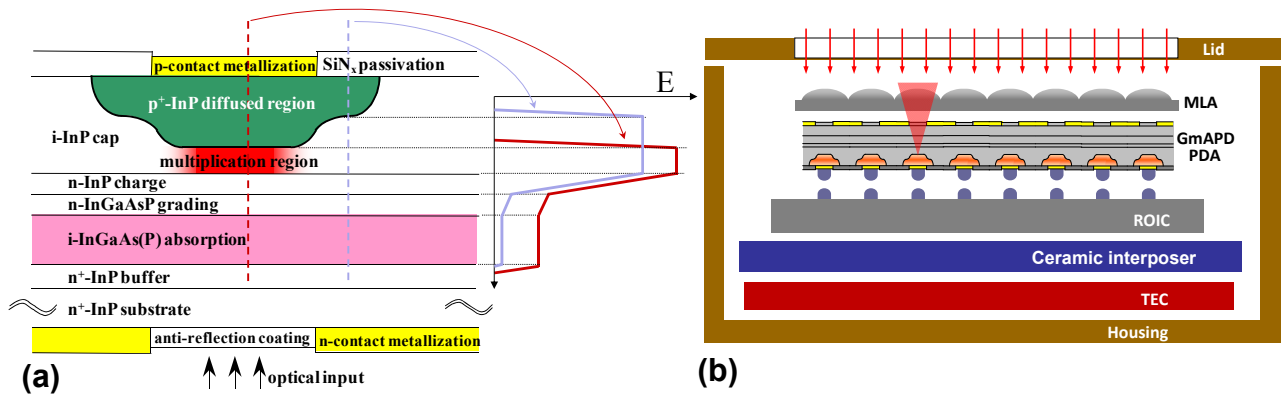


**Figure 1.** (a) Schematic cross-section of a planar-geometry diffused-junction GmAPD device structure illustrating the reduction of electric field amplitude at the edge of the device by tailoring of the diffusion profile to avoid edge breakdown effects. (b) Notional concept for a GmAPD focal plane array, consisting of the hybridized chip stack with readout integrated circuit (ROIC), Geiger-mode APD photodiode array (PDA), and microlens array (MLA) attached to a ceramic interposer for electrical signal routing and cooled by a thermoelectric cooler (TEC) in a hermetically sealed housing.

The ROICs incorporate on-chip clocks to control all timing operations. For results presented below, the 32 x 32 FPA ROIC used a phase-locked loop circuit, and the 32 x 128 FPA ROIC employed a ring oscillator circuit. Both FPAs achieve 13-bit timing resolution using 11-bit pseudorandom counters with two additional vernier bits created by using a copy of the clock with a 90 degree phase shift [1]. At the end of each range gate, frame data is scanned out using dedicated I/O ports. The 32 x 32 FPA has one I/O port for each of the 32 rows in the array, and scan circuitry achieves the read-out of the 32 pixels in each row in 3.36  $\mu$ s. The range gate duration is user-selectable with any value between 4 ns and 10  $\mu$ s. For a typical range gate duration of 2  $\mu$ s, the full frame duration of 5.36  $\mu$ s corresponds to a very high frame rate of 186 kHz. The 32 x 128 FPA also employs 32 I/O ports, with each port corresponding to four adjacent array columns read out in a serpentine fashion. By doubling the scan-out rate, the 128 pixels assigned to each I/O port are read out in just 6.72  $\mu$ s. In addition to the internally supplied clocks, both FPAs can be run with an external clock input for system synchronization. The initial 32 x 32 ROIC design was carried out in 0.18  $\mu$ m CMOS technology with circuit elements appropriately scaled to ensure forward compatibility with the 50  $\mu$ m pitch of the 32 x 128 ROIC.

### 2.3 Module design summary

Following the hybridization of the GmAPD PDA to the CMOS ROIC, we align and attach a GaP microlens array (MLA) to the exposed back surface of the PDA. Once the MLA has been attached to the PDA, the resulting chip stack of ROIC+PDA+MLA is attached to a ceramic interposer, which provides electrical routing of signals from the ROIC to the package interconnection pins. The interposer is then placed on a two-stage thermoelectric cooler (TEC), which has been previously mounted to the ceramic housing. Optical access to the chip stack is provided by an anti-reflection-coated sapphire window in the FPA lid, which is hermetically sealed to achieve reliable operation in harsh environments. A schematic illustration of this FPA architecture is given in Figure 1(b).

The solid body cut-away diagram in Figure 2(a) shows a scale model of the assembled module, including additional

elements such as a CuW heat sink and the housing pin grid array with 175 pins for electrical connections. As with the ROIC design, the design of this housing incorporated elements to ensure forward compatibility with the 32 x 128 FPA, and sensors of both formats utilize the same package housing elements. On the other hand, interposers must be circuit-specific. The photograph in Figure 2(b) illustrates a fully assembled 32 x 128 FPA module prior to lid attachment.

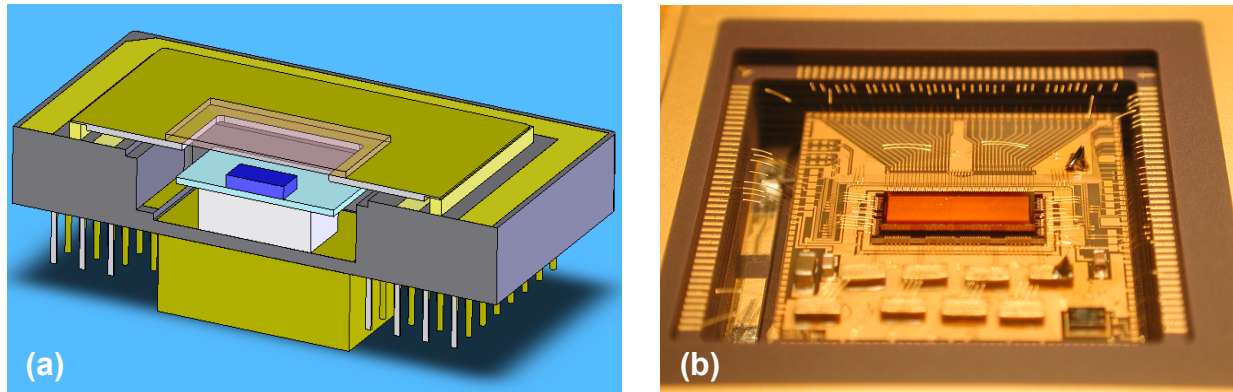


**Figure 2.** (a) Solid body model of FPA module with cut-away showing, from bottom to top, CuW heatsink (gold), ceramic package (gray), thermoelectric cooler (white), interposer board (light blue), hybridized ROIC+PDA+MLA chip stack (dark blue), and package window (clear). (b) Detailed photograph of fully assembled FPA module (without lid) shows 32 x 128 hybridized chip stack in center of interposer board.

### 3. DARK COUNT RATE AND PHOTON DETECTION EFFICIENCY PERFORMANCE

FPA sensors were characterized in a dark enclosure via computer control using FPGA-controlled electronics described elsewhere [5]. Photon detection efficiency (PDE) measurements were obtained with optical pulses focused to a single pixel or using broad illumination over an entire array. For array-level PDE characterization under broad illumination, the fiber source was collimated so that the optical intensity variation across the array was no more than  $\pm 5\%$ . Dark count rate (DCR) measurements were obtained with no illumination. Optical pulse timing could be set for pulse arrivals at any time within the selected range gate, and most data was acquired with pulse arrivals near the midpoint of a 2  $\mu\text{s}$  range gate. For single pixel illumination (e.g., for crosstalk measurements), the pulse intensity was typically attenuated to a mean photon number of  $\eta = 0.1$  so that the Poisson probability of there being two photons in any given pulse was less than 1%. For some measurements,  $\eta = 1$  was used to increase the data acquisition rate, in which case the resulting illuminated count measurements were corrected by assuming Poisson statistics to calculate the intrinsic PDE. To reduce statistical uncertainty in DCR and PDE measurements, most data presented below are based on the collection of at least 10,000 frames of data for the 32 x 32 FPAs and 5000 frames of data for the 32 x 128 FPAs.

#### 3.1 FPA-level mapping of dark count rate (DCR) and photon detection efficiency (PDE)

The most important characteristic of the GmAPD FPA is the fundamental tradeoff between DCR and PDE. Higher PDE can be achieved by operating the GmAPD array pixels at higher excess bias voltage, but only at the expense of increased DCR. The optimal operating point for managing this trade-off depends on various factors dictated by the specific imaging application. For example, for operation with high background count rates (such as daytime imaging), higher dark count rates will be tolerable as long as they do not exceed the background count rate, and operation at higher PDE will be desirable in such background-limited scenarios. Conversely, in dark conditions with no background, DCR will dominate the noise performance of the FPA, and a lower operating PDE may be optimal.

##### 3.1.1 DCR and PDE performance mapping for InGaAsP/InP 32 x 32 FPAs

To characterize the DCR and PDE performance of the GmAPD FPAs, we record array-level data to create performance maps of all pixels in the array. The maps in Figure 3 illustrate measurements for all 1024 pixels of a 32 x 32 FPA designed for detection at 1.06  $\mu\text{m}$ . Figure 3(a) illustrates DCR performance, with the quantitative value of DCR for each pixel indicated in kHz, and Figure 3(b) illustrates accompanying PDE performance, with quantitative values for each pixel indicated in percentage (%). Data were obtained at an operating temperature of 253 K and an excess bias

voltage of 3.5 V. These data demonstrate perfect yield, with 100% pixel operability and all pixels within target specifications for DCR and PDE performance.

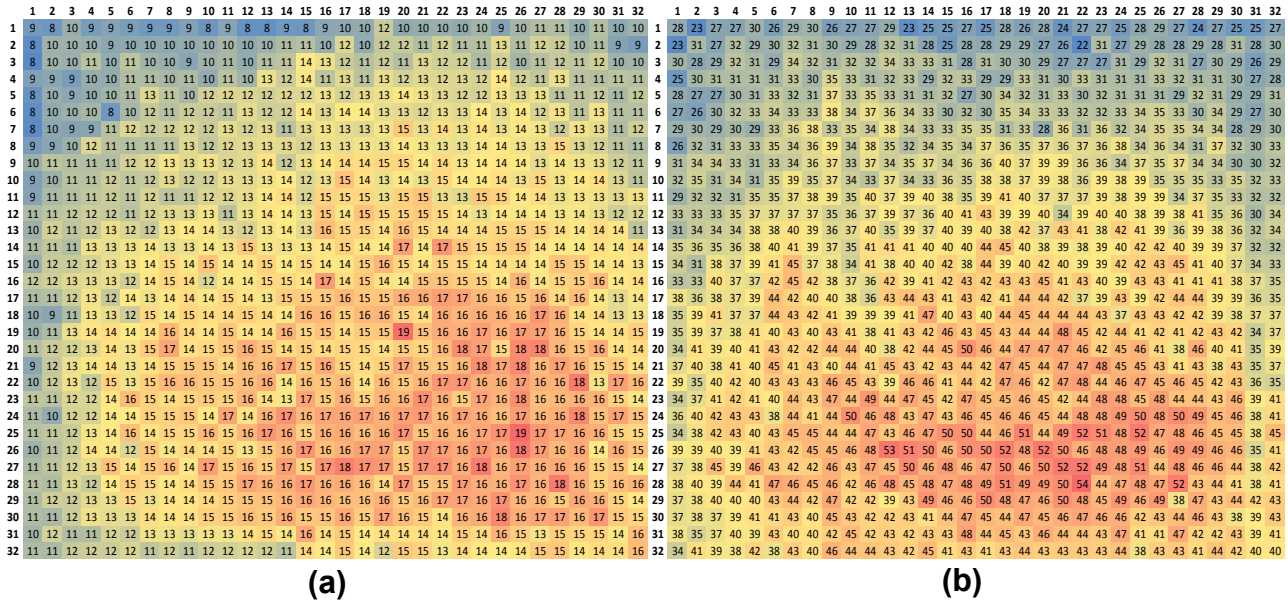


**Figure 3.** Performance maps of all 1024 pixels of a 32 x 32 InGaAsP/InP (1.06 μm) GmAPD FPA operating with an excess bias of 3.5 V at 253 K. (a) Dark count rate (DCR) in kHz for all pixels. All pixels are < 20 kHz; there are no high DCR pixels in this FPA. (b) Photon detection efficiency (PDE) in % for all pixels, where the average pixel PDE of 39% includes all optical losses related to the microlens array and other sources of insertion loss.

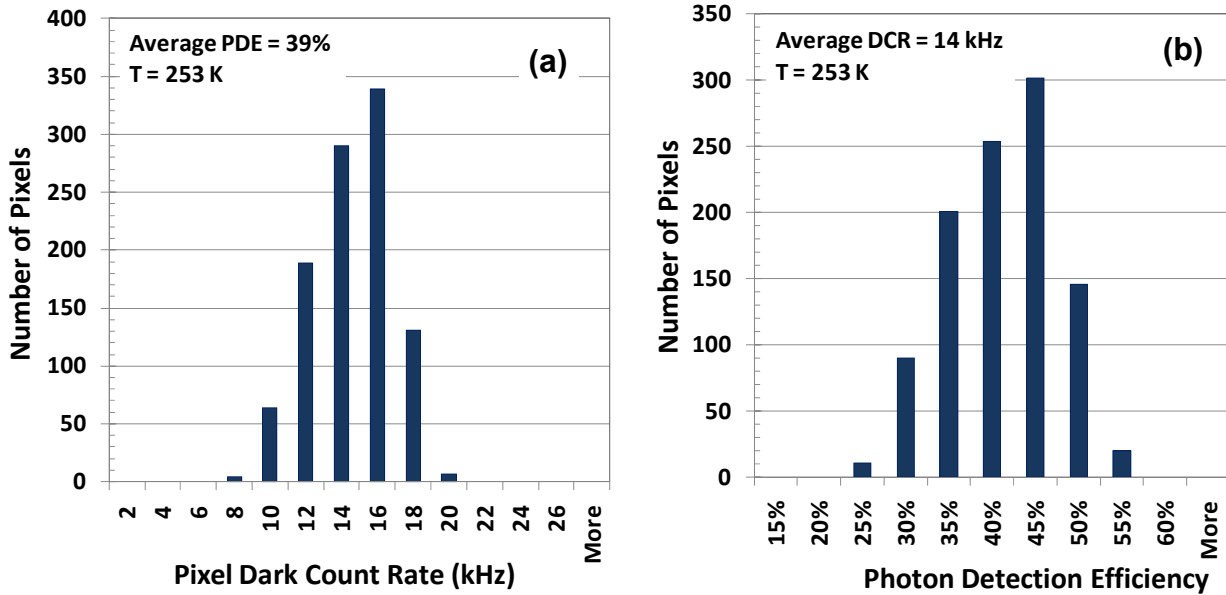


**Figure 4.** Histograms of (a) pixel dark count rates and (b) photon detection efficiencies for the map data presented in Figure 3 for InGaAsP/InP FPA at 1.06 μm. As the DCR histogram shows in (a), this FPA has no leaky or open pixels. The DCR distribution at 253 K has an average of 14 kHz with an rms deviation of 2.2 kHz. The corresponding PDE histogram in (b) has an average PDE of 39% with an rms deviation of 6%.

As shown in greater detail by the histogram in Figure 4(a), the DCR distribution for the entire 32 x 32 array has an average of 13.6 kHz and a standard deviation of 4.2 kHz. Additionally, all 1024 pixels in the array exhibit a DCR of less than 20 kHz for the specified operation conditions. In Figure 4(b), the average PDE for the entire array is 39%, and

the standard deviation of the distribution of PDE values is 6.3%. From the maps in Figure 3, it is apparent that variation in DCR and PDE across the array is quite systematic, with little random fluctuation. This suggests that non-uniformities are the result of systematic variation in device properties, with the most important factor being the variation in APD breakdown voltage  $V_b$ . Since a single applied voltage  $V_a$  is supplied to the entire array, the excess bias  $V_{ex} = V_a - V_b$  will vary among different pixels if they have different values of  $V_b$ . A smaller  $V_{ex}$  will result in smaller values for both DCR and PDE, and we see that the two variables tend to trend together at different locations across the array. We also note that the non-uniformity in PDE can be corrected using non-uniformity correction factors. However, in many applications, the FPA is scanned within the scene being imaged, and the scanning removes the impact of PDE non-uniformity without additional correction required.

### 3.1.2 DCR and PDE performance mapping for InGaAsP/InP 32 x 128 FPAs

As for the 32 x 32 FPAs described in the previous sub-section, we have characterized a 32 x 128 FPA to produce the performance maps of DCR and PDE illustrated in Figure 5. For this particular array, the FPA exhibits just 1 pixel with sufficiently high dark current that we deem it to be inoperable; all other pixels exhibit less than 55 kHz DCR. The PDE map shows that two pixels along the bottom edge of the array show spurious (high) values, although the DCR values for these pixels are not excessively high. Categorizing these 3 pixels to be inoperable, this FPA has >99.9% pixel operability. Because this FPA did not have a microlens array (MLA), the PDE values reported in Figure 5(b) are obtained by considering only the broad illumination photons falling within the active region of each pixel; i.e., PDE is not burdened by low fill factor of the array in the absence of the MLA. We present this in this way to show the “active-region” PDE performance. The PDE performance with MLAs is expected to be ~70% of the active-region values. (For the 32 x 32 FPAs, we have found ~75% fill factor with MLAs.)



**Figure 5.** Performance maps of all 4096 pixels of a 32 x 128 InGaAsP/InP (1.06  $\mu\text{m}$ ) GmAPD FPA operating with an excess bias of 2.25 V at 248 K. (a) Dark current density (in kHz) for all pixels shows just 1 high DCR pixel. (b) Photon detection efficiency (in %) for all pixels is reported only for photons hitting the active regions since a microlens array was not present. Two pixels exhibit spurious (high) PDE measurements. Overall pixel operability is >99.9%.

More details of the DCR and PDE performance distributions from the maps in Figure 5 are evident in the histograms of these data shown in Figure 6. For the DCR distribution in Figure 6(a), the mean DCR is 3.7 kHz and the standard deviation is 3.4 kHz. For the PDE distribution, the mean active-region PDE is 34% and the standard deviation is 9%. These distributions are broader than those found for the 32 x 32 FPAs (see Figure 4), and the maps in Figure 5 clearly show that there is a substantial systematic variation in both DCR and PDE along the long dimension of the FPA. This

systematic variation can be correlated to the precise location of this PDA on the InGaAsP/InP wafer: this particular PDA was oriented with its long direction exactly parallel to the radius of the wafer and located approximately midway between the wafer center and the wafer edge. At this location, wafer-level variations in epitaxial layer thickness and doping are relatively pronounced due to the details of the epitaxial growth process. To show the impact of these details pertaining to epitaxial growth uniformity, we show the DCR map of another FPA in Figure 7 for which the PDA was located very close to the wafer center. For this FPA, the DCR shows better uniformity in the long direction; for the bias voltage used, the mean DCR was 26 kHz with a standard deviation of 10 kHz. Additionally, although about 20 pixels show elevated DCR between 100 and 175 kHz, these would still be usable in many circumstances, in which case this array provides 100% pixel operability from the perspective of DCR. (For this module, FPA-level PDE was degraded by MLA misalignment.) This dependence of performance uniformity on epitaxial growth characteristics becomes more important as the absolute dimensions of the GmAPD PDAs increase. The long dimension of the 32 x 128 FPA is 6.4 mm (given 128 pixels at 50  $\mu\text{m}$  pitch) while the dimensions of the 32 x 32 FPA are only 3.2 mm.

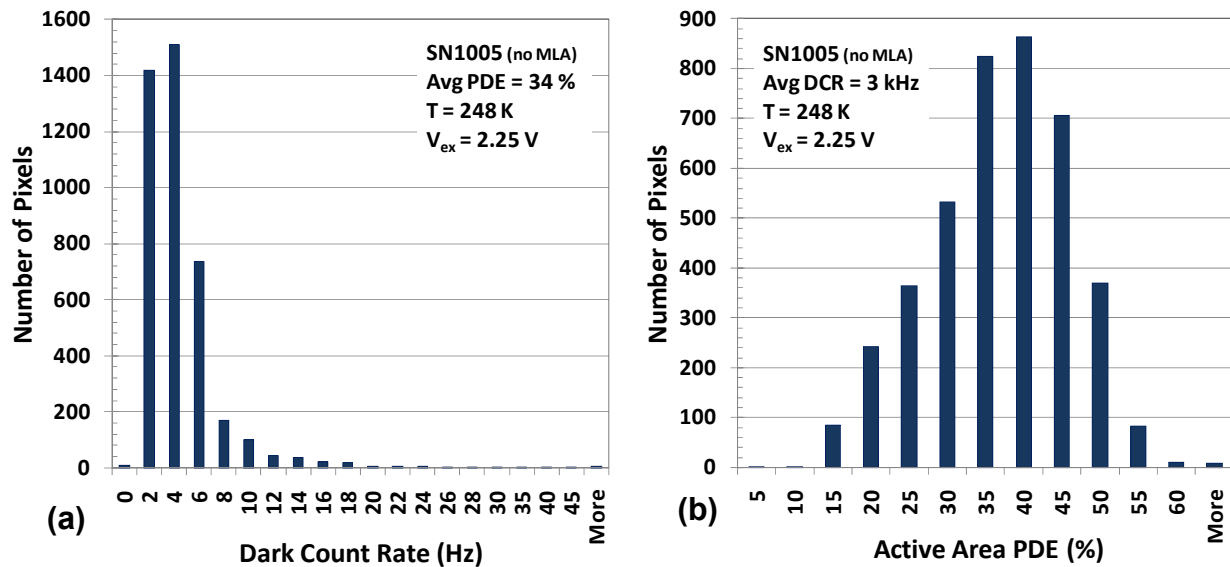


**Figure 6.** Histograms of (a) pixel dark count rates and (b) active area photon detection efficiencies for the map data presented in Figure 5 for InGaAsP/InP FPA at 248 K. Although about 20 pixels have elevated DCR (100 to 175 kHz), the average DCR is 3.7 kHz with an rms deviation of 3.4 kHz. The corresponding PDE histogram (which is corrected for fill factor losses since no microlens array is present) in (b) has an average active area PDE of 34% with an rms deviation of 9%.

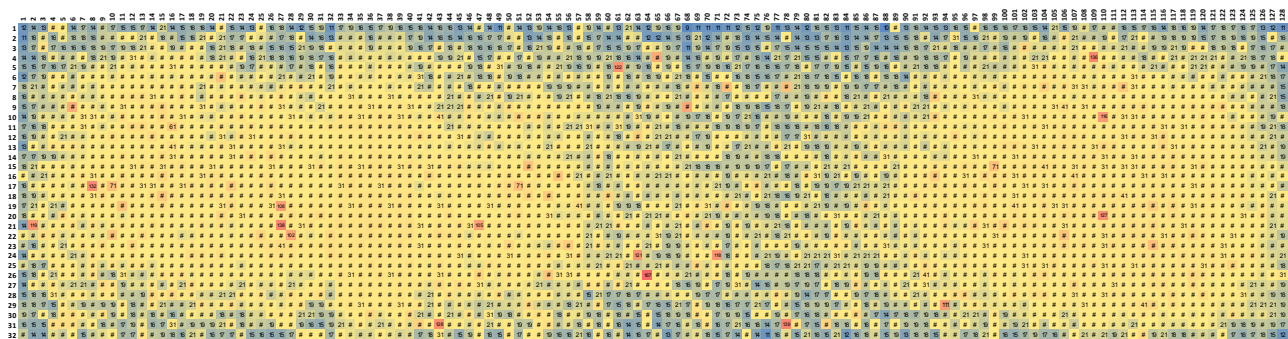


**Figure 7.** Dark count rate (in kHz) performance map for all pixels of a 32 x 128 FPA that shows better uniformity than the map shown in Figure 5; see text for discussion. Moreover, this array exhibits 100% pixel operability; about 20 pixels have elevated DCR (100 to 175 kHz) but are still operable.

### 3.2 Comparison of DCR vs. PDE performance for 32 x 32 and 32 x 128 FPAs

As described above, the relationship between DCR and PDE presents the most fundamental tradeoff in GmAPD

operation. To illustrate this relationship in more detail, we have plotted in Figure 8(a) the dependence of DCR on PDE for a random selection of pixels from the 32 x 32 FPA maps in Figure 3, and in Figure 8(b) the dependence of DCR on PDE for random pixels from the 32 x 128 FPA maps in Figure 5. Specific points on a DCR vs. PDE curve are obtained by measuring these two parameters at specific values of the excess bias voltage. For the 32 x 32 FPA, although there is some variation among these pixels, at any given value of PDE, they all exhibit DCR values consistent to within a factor of  $\sim 2$ . This behavior represents greater consistency than is apparent in the full-array performance maps in Figure 3 because the mapping data includes the additional variation imposed by spatial non-uniformities in  $V_b$  (and therefore  $V_{ex}$ ) across the array. For the DCR vs. PDE curves, since both parameters are measured at the same  $V_{ex}$  for a given pixel, array-level variation in  $V_{ex}$  is not a factor.

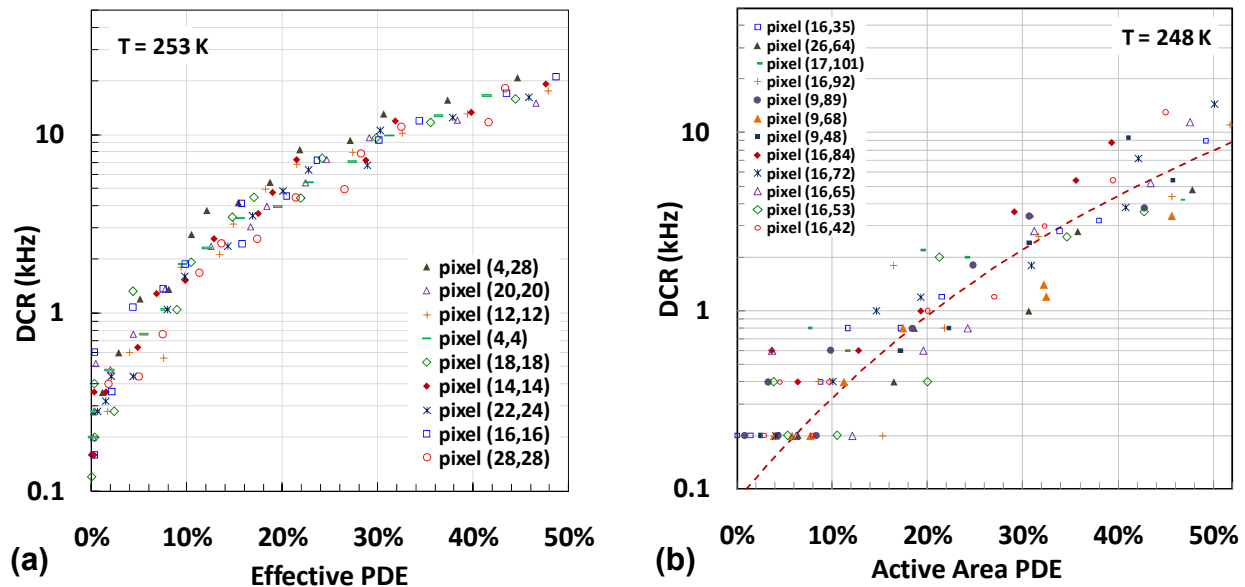


**Figure 8.** Dependence of DCR on PDE for a random sample of pixels from (a) the 32 x 32 FPA with performance maps in Figure 3 and (b) the 32 x 128 FPA with performance maps in Figure 5. Regardless of position on the FPA, pixels show consistent DCR vs. PDE behavior, although the 32 x 128 FPA exhibits larger variation. The dashed curve in (b) indicates the median behavior.

The DCR vs. PDE curves for the 32 x 128 FPA shown in Figure 8(b) are qualitatively similar to those found for the 32 x 32 FPA, although they exhibit somewhat greater fluctuations—as large as a factor of  $\sim 5$ . The median DCR vs. PDE performance is indicated by the dashed line in the figure. The difference in DCR values at a given PDE for the two array formats can be approximately reconciled by considering several factors: (i) the 32 x 128 PDE values are not burdened by a fill factor (as explained above), while the 32 x 32 PDE values include all optical losses, dominated by the 75% MLA fill factor; (ii) the smaller active area of the 32 x 128 pixels should reduce DCR by a factor of  $\sim 3.5$ ; and (iii) the 5 K lower operating temperature of the 32 x 128 FPA will reduce DCR by  $\sim 30\%$ . The first factor above dictates that if we consider the 32 x 32 FPA DCR of  $\sim 10$  kHz at a 30% “effective” PDE, then we should compare the 32 x 128 FPA DCR of  $\sim 4$  kHz at a 40% “active-area” PDE. The second and third factors predict that the 32 x 128 DCR performance should be a factor of 5 lower than the 32 x 32 DCR, and the actual difference of a factor of 2.5 suggests that the 32 x 32 FPA device quality is somewhat better than that of the 32 x 128 FPA. Nevertheless, this comparison yields consistent results within expected lot-to-lot performance variations.

#### 4. CROSSTALK CHARACTERIZATION

Another GmAPD FPA performance parameter of considerable importance to 3D imaging applications is crosstalk. The detection of single photons in GmAPDs involves macroscopic current flows that can cause optical crosstalk due to hot carrier luminescence, in which the acceleration of charge in a high-field avalanche region gives rise to photon emission at the rate of one photon per  $10^5 - 10^6$  carriers that flow through the avalanche region. Because all pixels of the FPA are sensitive to single photons, the coupling of emitted photons to neighboring active areas can cause correlated spurious

dark counts at these neighbors that are defined as crosstalk events. With reference to Figure 9(a), luminescent photon emission can couple from an avalanching pixel to a nearest neighbor pixel by direct “line-of-sight” paths or to more distant neighbors by back-reflection from the rear surface of the GmAPD chip. Etched trenches between nearest neighbor pixels are fabricated to reduce the probability for direct line-of-sight coupling.

Crosstalk characterization can be obtained from wafer-level frame data for avalanches of any origin, so dark or lit measurements can be used [7]. Spatial correlations between avalanches are readily determined from pixel positions, and temporal correlations are provided by the pixel-level timestamp data. To obtain the crosstalk data illustrated in Figure 9(b), we induced avalanche events in a specific “trigger” pixel using focused single photon illumination and then searched the data for pixels surrounding the illuminated pixel to find temporally correlated avalanche events. We have found that almost all correlated crosstalk events occur within 5 ns of the trigger-pixel avalanche and that no correlated events (i.e., above the DCR level) are found with a latency of more than 10 ns. The data in Figure 9(b) show per-pixel crosstalk probability for a 32 x 32 FPA as a function of distance from the triggering pixel (in units of the 100 μm pitch). The data show a decrease in crosstalk with increasing interpixel distance  $D$  that is roughly consistent with an expected  $1/D^2$  rolloff, although there is non-monotonic behavior that depends quite sensitively on the precise location of a particular crosstalk pixel. The details of this non-monotonic behavior are most strongly dependent on the strength of optical reflections by total internal reflection at the back surface of the PDA that couple photons emitted by the trigger photon to specific neighboring pixels.

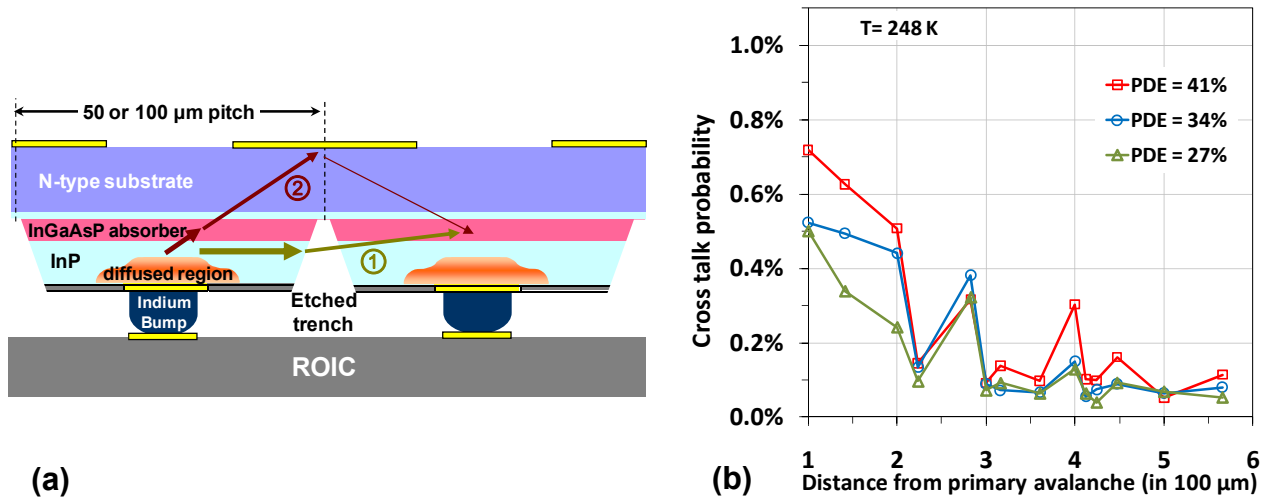


**Figure 9.** (a) Schematic illustration of two principal optical crosstalk mechanisms in GmAPD PDAs. Hot carrier luminescence during an avalanche in the left-hand pixel may emit photons that reach nearest-neighbors by line-of-sight paths or further neighbors by reflection from the rear surface of the PDA. (b) Measured crosstalk probability per pixel as a function of distance from the “trigger” avalanche pixel for 32 x 32 FPAs with 100 μm pitch.

As illustrated schematically in Figure 9(a), the PDA back surface has an opaque metallic coating outside the immediate vicinity of the active region, while immediately above the active region, an anti-reflection (AR) coating is deposited to provide low-loss transmission of the input photons from the microlens array. We have chosen a metallic film that helps to attenuate reflections. However, the strength of the reflections at the AR-coated regions can not be reduced without degrading the transmission of the input signal. Therefore, any crosstalk path that involves a reflection from a non-metallized AR-coated region will have relatively larger crosstalk. This is exactly what we see for non-line-of-sight crosstalk for neighbors at the following distances: two pixels away (reflection from the AR coating of the nearest neighbors); 2.8 pixels away (reflection from the AR coating of the nearest diagonal neighbors); and four pixels away (reflection from 2<sup>nd</sup> nearest horizontal and vertical neighbors). This hypothesis is confirmed by the very weak crosstalk observed for neighbors that require a reflection from the metal-coated surface, such as the neighbors at a distance of 2.2 pixels (a knight’s move in chess) or of three pixels. In considering the cumulative crosstalk behavior, the total integrated crosstalk probability  $P_{tot}$ —i.e., the probability that any crosstalk event takes place at any pixel in response to a primary avalanche—is under 15% when FPA-level PDE ~ 35%. For many applications, a single crosstalk event can be tolerated, and so the probability of more than one crosstalk event  $P(>1)$  in response to a primary avalanche is of interest. For the data in Figure 9(b),  $P(>1) \sim 2\%$  when PDE ~ 35%.

Crosstalk events are of potentially greater concern for the 32 x 128 format FPAs given that their pixel pitch of 50  $\mu\text{m}$  is half that of the 100  $\mu\text{m}$  pitch 32 x 32 FPAs. The data in Figure 10(a) show per-pixel crosstalk probability for a 32 x 128 FPA as a function of distance in units of pixel pitch (in this case 50  $\mu\text{m}$ ), analogous to the data in Figure 9(b) for a 32 x 32 FPA. Qualitatively, the data are very comparable, with similar non-monotonic peaks at distances that involve reflections from AR coated regions (e.g., at distances of 4 and 6 pixels), and even quantitatively, both types of arrays exhibit nearest-neighbor cross talk probability of  $\sim 0.5 - 1\%$ , with further neighbors having  $\sim 0.1 - 0.3\%$ . The much greater number of neighbors for the 32 x 128 format within a given absolute radius (e.g., 500  $\mu\text{m}$ ) results in somewhat higher cumulative crosstalk metrics, which are summarized in Figure 10(b). This figure shows the probability  $P(n)$  of finding a given number of crosstalk events  $n$  in response a triggering avalanche.

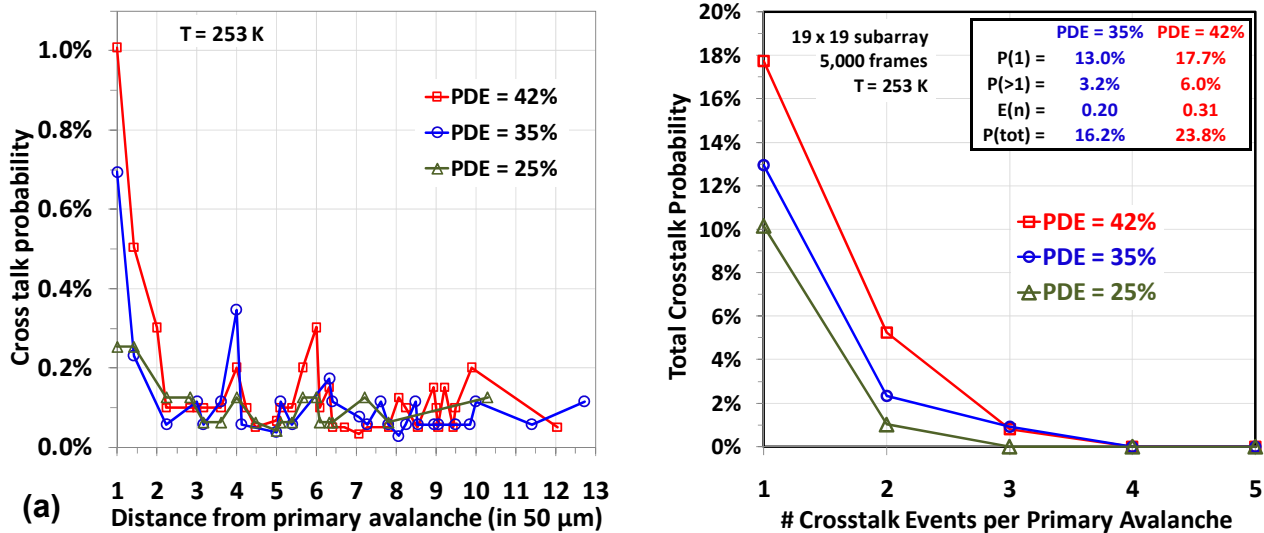


**Figure 10.** (a) Measured crosstalk probability per pixel as a function of distance from the primary avalanche pixel for 32 x 128 FPAs with 50  $\mu\text{m}$  pitch. (b) Cumulative crosstalk probability for different numbers of crosstalk events per primary avalanche. Inset table summarizes cumulative crosstalk metrics described in text.

#### 4. TIMING JITTER CHARACTERIZATION

In any LADAR system, the accuracy with which the range of an object can be determined is limited by the total uncertainty in the measurement of the roundtrip time-of-flight between the sensor and the object. The contribution of the FPA to this total uncertainty, commonly referred to as the timing jitter, is an important characteristic of the FPA performance. For optical pulses that nominally arrive at the FPA at precisely the same time within successive range gates, an FPA with perfect timing characteristics will always register a count in the same time bin (i.e., with the same timestamp). However, finite timing jitter can cause counts to occur in different bins from one frame to the next.

To characterize the jitter of our GmAPD FPAs, we have employed an over-sampling technique that is similar to approaches used with digital sampling oscilloscopes and eye-diagram analyzers for communications links. In Figure 11(a), we present a simple illustration of the concept. The top panel shows the response of the FPA with a nominal photon arrival occurring precisely in the center of time bin  $N$ . Although most counts are registered in time bin  $N$ , the finite timing jitter of the FPA causes some fraction of the counts to register in time bins  $N-1$  and  $N+1$ , indicated by solid red circles. The lower panel illustrates a second set of measurements with the nominal photon arrival shifted by 2.5 time bins, in which case most counts occur in either of time bins  $N+2$  and  $N+3$ , but some occur in  $N+1$  and  $N+4$ , as indicated by open green circles. The basic procedure of the over-sampling analysis is to shift the data for the second set of measurements by a temporal offset that is exactly equal and opposite to the shift in the photon arrival time (i.e., 2.5 time bins in this example). After shifting the second set of measurements to the solid green circles, the combination of the solid red and green circles comprises a more detailed description of the timing probability distribution function (PDF). In the simple example illustrated by Figure 11(a), just two different photon arrival times are used, but the same principle can be applied for a larger number of time shifts to construct a more detailed PDF.

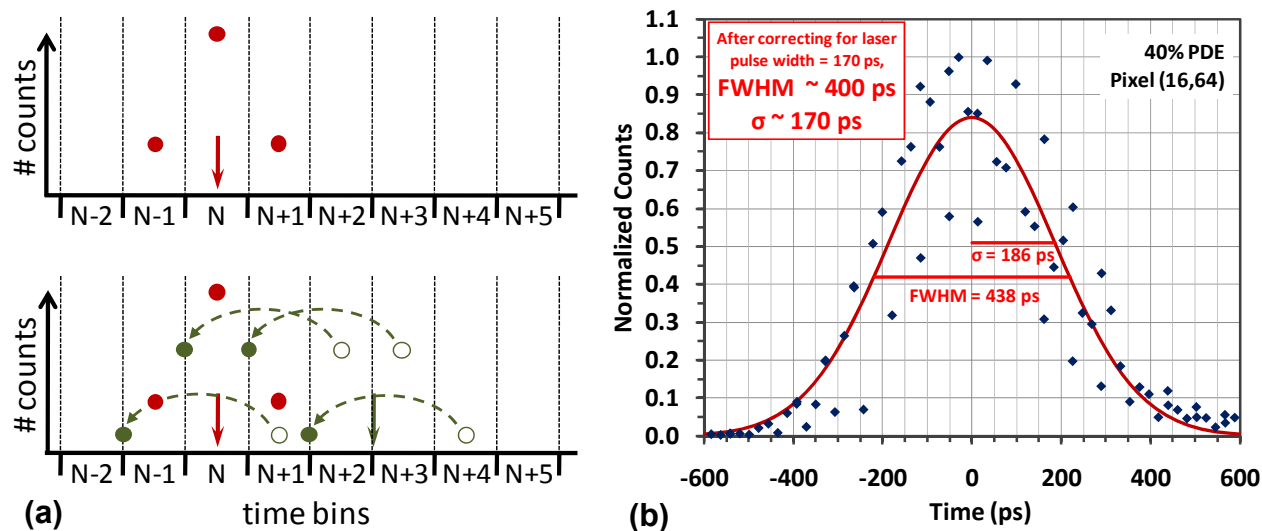


**Figure 11.** (a) Illustration of timing jitter measurement technique; see text for discussion. (b) Experimental results for a 32 x 128 FPA using the oversampling technique illustrated in (a) with 64 ps timing offsets. After subtraction of the FWHM laser pulse width of ~170 ps, the rms jitter is found to be ~170 ps.

To employ the over-sampling technique just described, we used up to 14 time shifts in multiples of 64 ps by introducing reproducible delays in the drive signal to the pulsed laser. Therefore, for each successive time shift, the laser pulse arrived with successive 64 ps delays relative to the beginning of each range gate. This allowed us to step the photon arrival through several consecutive time bins, with the nominal photon arrival times occurring at different points within these time bins. By “folding back” the data sets obtained for the delayed photon arrivals by the corresponding time shift used for each set, we obtained the PDF illustrated by the blue data points in Figure 11(b). The solid red curve is the best Gaussian fit to the measured data points. In addition to the inherent timing jitter of the FPA, the measured PDF includes other sources of timing uncertainty in our test set. The dominant contribution to this test system jitter was the 170 ps full-width at half-maximum (FWHM) of our laser pulses. After compensation for the laser pulse width, we find that the Gaussian fit indicates a jitter of ~400 ps based on a FWHM criterion, and ~170 ps for a root-mean-square jitter.

## 5. CONCLUSIONS

In this paper, we have described the performance of focal plane arrays based on Geiger-mode APDs with single photon sensitivity that function as sensor engines for 3-D LADAR imaging systems. We have reported results for the first such FPAs based on planar-geometry GmAPDs for a 32 x 128 format with 50  $\mu\text{m}$  pitch. These new results have been compared to results obtained for 32 x 32 format FPAs with 100  $\mu\text{m}$  pitch designed on the same technology platform. We have shown that we can achieve excellent yield for high pixel operability in both formats. The larger arrays are subject to somewhat greater variation in their performance characteristics as a function of pixel position on the array due to non-uniformities in the epitaxial growth process. Additionally, although the 32 x 128 FPAs exhibit somewhat larger fluctuation in their pixel-level DCR vs. PDE performance, the overall quality of these pixels is comparable to those on 32 x 32 FPAs.

Crosstalk due to hot carrier luminescence during avalanche events also shows strong similarities between the two formats. Nearest-neighbor direct line-of-sight coupling dominates and results in similar per-pixel crosstalk probabilities of ~0.5 – 1%. For both formats, the strength of coupling to further neighbors is strongly dependent on the intensity of photon reflections from the back surface of the PDA. Overall, for operation at a given PDE, the various crosstalk metrics—such as total integrated crosstalk  $P_{\text{tot}}$  and the probability  $P(>1)$  for more than one simultaneous crosstalk event—appear to be moderately higher for the 32 x 128 FPAs than they are for the 32 x 32 FPAs. We can achieve reductions in crosstalk for both formats in the future by using appropriate epitaxial absorbing layers to attenuate crosstalk photons with a wavelength shorter than that of the imaging photons.

Finally, timing jitter characterization for the 32 x 128 FPAs yields jitter performance of about 400 ps based on a FWHM criterion and 170 ps based on an RMS criterion. These values represent somewhat lower performance than jitter data of ~265 ps FWHM and ~100 ps RMS obtained from 32 x 32 FPAs [6]. Most likely, this difference is dominated by the different clock circuits for the two different formats: a phase-locked loop for the 32 x 32 FPA, and a ring oscillator for the 32 x 128 FPA.

## ACKNOWLEDGMENTS

We are grateful to Dr. Monte Turner for his support throughout this work, for which we wish to acknowledge funding from DARPA. We also greatly appreciate the collaborative efforts of many colleagues at MIT Lincoln Laboratory, including Gary Smith, Alex McIntosh, Simon Verghese, Brian Aull, Brian Tyrrell, and Joe Funk.

## REFERENCES

- [1] B. F. Aull, A. H. Loomis, D. J. Young, R. M. Heinrichs, B. J. Felton, P. J. Daniels, D. J. Landers, "Geiger-mode avalanche photodiodes for three-dimensional imaging," *MIT Lincoln Laboratory Journal*, vol. 13, no. 2, p. 335 – 350 (2002).
- [2] B. F. Aull, A. H. Loomis, D. J. Young, *et al.*, "Three-dimensional imaging with arrays of Geiger-mode avalanche photodiodes," *Proceedings of the SPIE* 5353, p. 105 – 116 (2004).
- [3] M. A. Albota, B. F. Aull, D. G. Fouche, *et al.*, "Three-dimensional imaging laser radars with Geiger-mode avalanche photodiode arrays," *MIT Lincoln Laboratory Journal*, vol. 13, no. 2, p. 351 – 370 (2002).
- [4] M. A. Itzler, X. Jiang, M. Entwistle, K. Slomkowski, M. Owens, A. Tosi, F. Acerbi, F. Zappa, and S. Cova, "Advances in InGaAsP-based avalanche diode single photon detectors," *J. Modern Optics* **58**, Nos. 3–4, 174 – 200 (2011).
- [5] M. A. Itzler, M. Entwistle, M. Owens, K. Patel, X. Jiang, K. Slomkowski, S. Rangwala, P. F. Zalud, T. Senko, J. Tower, J. Ferraro, "Geiger-mode avalanche photodiode focal plane arrays for three-dimensional imaging LADAR," *Proceedings of the SPIE* **7808**, 78080C (2010).
- [6] M. A. Itzler, M. Entwistle, M. Owens, K. Patel, X. Jiang, K. Slomkowski, S. Rangwala, P. F. Zalud, T. Senko, J. Tower, J. Ferraro, "Design and performance of single photon APD focal plane arrays for 3-D LADAR imaging," *Proceedings of the SPIE* **7780**, 77801M (2010).
- [7] M. A. Itzler, M. Entwistle, M. Owens, X. Jiang, K. Patel, K. Slomkowski, T. Koch, S. Rangwala, P. F. Zalud, Y. Yu, J. Tower, J. Ferraro, "InP-based Geiger-mode avalanche photodiode arrays for three-dimensional imaging at 1.06  $\mu\text{m}$ ," *Proceedings of the SPIE* **7320**, 73200O (2009).
- [8] S. Verghese, J. P. Donnelly, E. K. Duerr, *et al.*, "Arrays of InP-based Avalanche Photodiodes for Photon Counting," *IEEE Sel. Topics in Quantum Electron.* vol. 13, p. 870 – 886 (2007).
- [9] M. A. Itzler, R. Ben-Michael, C.-F. Hsu, K. Slomkowski, A. Tosi, S. Cova, F. Zappa, and R. Ispasoiu, "Single photon avalanche diodes (SPADs) for 1.5  $\mu\text{m}$  photon counting applications," *J. Mod. Opt.*, vol. 54, no. 2-3, pp. 283-304 (2007).
- [10] M. A. Itzler, X. Jiang, R. Ben-Michael, K. Slomkowski, M. A. Krainak, S. Wu, and X. Sun, "InGaAsP avalanche photodetectors for non-gated 1.06  $\mu\text{m}$  photon-counting receivers," *Proceedings of the SPIE* 6572, 65720G (2007).
- [11] X. Jiang, M. A. Itzler, R. Ben-Michael, K. Slomkowski, "InGaAsP/InP Avalanche Photodiodes for Single Photon Detection," *IEEE J. of Sel. Topics in Quantum Electronics* 13, p. 895 – 905 (2007).
- [12] X. Jiang, M. A. Itzler, R. Ben-Michael, K. Slomkowski, M. A. Krainak, S. Wu, and X. Sun, "Afterpulsing effects in free-running InGaAsP single photon avalanche diodes," *IEEE J. Quantum Electron.*, vol. 44, p. 3 – 11 (2008).
- [13] K. Nishida, K. Taguchi, and Y. Matsumoto, "InGaAsP heterostructure avalanche photodiodes with high avalanche gain," *Appl. Phys. Lett.*, vol. 35, 251–252 (1979).
- [14] M. A. Itzler, K. K. Loi, S. McCoy, N. Codd, N. Komaba, "High-performance, manufacturable avalanche photodiodes for 10 Gb/s optical receivers," *Proc. of 25<sup>th</sup> Optical Fiber Communication Conference (OFC 2000)*, Vol. 4, p. 126–128 (2000).
- [15] Y. Liu, S. R. Forrest, J. Hladky, M. J. Lange, G. H. Olsen, D. E. Ackley, *J. Lightwave Tech.*, vol. 10, 182 (1992).